

The Physical Characteristics of Interstellar Medium in NGC 3665 with *Herschel* Observations*

Meng-Yuan Xiao^{1,2,5}, Yinghe Zhao^{3,4,6}, Qiu-Sheng Gu^{1,2,5}, Yong Shi^{1,2,5}

¹ *School of Astronomy and Space Science, Nanjing University, Nanjing 210093,
P. R. China;*

qsgu@nju.edu.cn

² *Key Laboratory of Modern Astronomy and Astrophysics, Nanjing University, Nanjing
210093, P. R. China*

³ *Yunnan Observatories, CAS, Kunming 650011, P. R. China*

⁴ *Key Laboratory for the Structure and Evolution of Celestial Objects, CAS, Kunming
650011, P. R. China*

⁵ *Collaborative Innovation Center of Modern Astronomy and Space Exploration, Nanjing
210093, P. R. China*

⁶ *Center for Astronomical Mega-Science, CAS, 20A Datun Road, Chaoyang District,
Beijing 100012, P. R. China*

ABSTRACT

We present the analysis of the physical properties of the interstellar medium (ISM) in the nearby early-type galaxy NGC 3665, based on the far-infrared (FIR) photometric and spectroscopic data as observed by the *Herschel* Space Observatory. The fit to the spectral energy distribution reveals a high dust content in the galaxy, with the dust-to-stellar mass ratio of $M_{\text{dust}}/M_* \sim 1.1 \times 10^{-4}$ that is nearly three times larger than the mean value of local S0+S0a galaxies. For the ionized regions (H II regions), the electron density (n_e) is around $49.5 \pm 11.9 \text{ cm}^{-3}$ based on the $[\text{N II}] 122 \mu\text{m}/[\text{N II}] 205 \mu\text{m}$ ratio. For the photodissociation regions, the heating efficiency is in the range of 1.26×10^{-3} and 1.37×10^{-3} based on the $([\text{C II}] + [\text{O I}] 63 \mu\text{m})/L_{\text{TIR}}$, which is slightly lower than other local galaxies; the hydrogen nucleus density and the strength of FUV radiation field

**Herschel* is an ESA space observatory with science instruments provided by European-led Principal Investigator consortia and with important participation from NASA.

are $n \sim 10^4 \text{ cm}^{-3}$ and $G_0 \sim 10^{-0.25}$, respectively. The above results are consistent with the presence of weak AGN and a low level of star-forming activity in NGC 3665. Our results give strong support to the ‘morphological quenching’ scenario, where a compact, massive bulge can stabilize amount of cool gas against star formation.

Subject headings: galaxies: individual (NGC 3665) – galaxies: elliptical and lenticular, cD – galaxies: ISM – infrared: ISM – ISM: lines and bands

1. Introduction

Interstellar medium (ISM) plays a crucial role in the galaxy formation and evolution. It is the primary reservoir for star formation. The mutual interaction between ISM and stars determines the rates of both gaseous depletion and star formation in the galaxy. ISM contains several main components: ionized gas, neutral gas, cold molecular clouds, as well as dust grains. When molecular clouds collapse under their own gravity to form stars, the gravity is required to overcome the random motion pressure, which requires the interstellar gas to be cooled down sufficiently. Neutral and ionized gas can be heated up by the photoelectric process (PE; Tielens & Hollenbach 1985), and cooled via collisional excitation of C^+ , O, N^+ and other elements. The atomic fine-structure emission lines in the far-infrared (FIR), such as $[\text{N II}]$ 122 and 205 μm , $[\text{C II}]$ 158 μm , $[\text{O I}]$ 63 μm , and $[\text{C I}]$ 370 μm , are very important coolants, which play a crucial role in the thermal balance in the H II regions and photodissociation regions (PDRs), and can be served as critical diagnostic tools for studying the physical properties of ISM (e.g., Kaufman et al. 1999).

Among these fine-structure lines, $[\text{C II}]$ 158 μm is the brightest and the dominant FIR cooling line, typically accounting for 0.1%-1% of the total FIR luminosity (Stacey et al. 1991; Malhotra et al. 2001; Díaz-Santos et al. 2013; Sargsyan et al. 2014). The ionization potential of carbon is 11.26 eV, thus the $[\text{C II}]$ line can be a tracer of both ionized and neutral gas. The $[\text{O I}]$ emission originates in the PDRs since the ionization potential of oxygen is just above 13.6 eV, whereas the $[\text{N II}]$ line exclusively arises from the ionized gas as nitrogen has an ionization potential of 14.5 eV. As shown in previous studies (Zhao et al. 2013, 2016a; Sargsyan et al. 2014), both $[\text{N II}]$ 205 μm and $[\text{C II}]$ 158 μm lines can be served as useful indicators of star formation rate (SFR). Based on the critical densities of collisional excitations for $[\text{N II}]$ 122 and 205 μm , $\sim 293 \text{ cm}^{-3}$ and 44 cm^{-3} at the electron temperature of 8000 K, respectively, the $[\text{N II}]$ 122/ $[\text{N II}]$ 205 ratio is a sensitive probe of the electron density ($10 \lesssim n_e \lesssim 300 \text{ cm}^{-3}$) of ionized gas, which can be further used to estimate the fraction of $[\text{C II}]$ 158 μm originating from ionized gas (Oberst et al. 2006, 2011).

Based on *Infrared Space Observatory* (*ISO*) observations, Malhotra et al. (2000) investigated the physical properties of gas and dust in four elliptical/S0 galaxies, and proposed that softer radiation field might result in lower $[\text{C II}]/F_{\text{FIR}}$ ratios than those of normal star-forming galaxies by a factor of 2 – 5. With data of *Herschel Space Observatory* (hereafter *Herschel*; Pilbratt et al. 2010), Lapham et al. (2017) presented spectroscopic observations of the FIR emission lines in 20 nearby elliptical/S0 galaxies and found that the average of $[\text{C II}]/F_{\text{FIR}}$ ratio is slightly lower than that of spiral galaxies, and $[\text{C II}]$ luminosity can be served as a good SFR tracer for both early-type galaxies (ETGs) and spirals. Furthermore, Lapham et al. (2017) showed that the fraction of $[\text{C II}]$ emission arising from ionized gas is similar in ETGs (63.5 %) and normal spirals (53.0 %).

In this work, we investigate the ISM properties of a nearby ETG, NGC 3665. In general, ETGs in the local Universe contain very little cool gas and/or dust. Many studies focused on the mechanisms of star formation suppression for nearby ETGs, such as removing cool gas (Di Matteo et al. 2005; Hopkins et al. 2006), suppressing gas infall and cooling (Birnboim & Dekel 2003; Croton et al. 2006; Lanz et al. 2016), or stabilizing gas reservoirs (Martig et al. 2009; Tacchella et al. 2015), etc. However, several recent works have shown that $\sim 40\%$ elliptical and S0 galaxies are rich in both dust and cool gas (Temi et al. 2007a,b; Young et al. 2011, 2014; Alatalo et al. 2013), with the SFR reaching a few $M_{\odot} \text{ yr}^{-1}$ (Temi et al. 2009a,b).

NGC 3665 ($11^{\text{h}}24^{\text{m}}43^{\text{s}}.7$, $+38^{\circ}45'46''$) is located 33.1 Mpc away (Cappellari et al. 2011), with an inclination angle, i , of 69.9° (Onishi et al. 2017), and Hubble type of SA0 (RC3; de Vaucouleurs et al. 1991). It is found to be gas-rich in the center (Young et al. 2011; Serra et al. 2012; Alatalo et al. 2013; Davis et al. 2013, 2014; Kamenetzky et al. 2016; Nyland et al. 2016; Onishi et al. 2017), with a total molecular gas mass of $10^{9.11 \pm 0.01} M_{\odot}$ from the Combined Array for Research in Millimeter Astronomy (CARMA) observations (Alatalo et al. 2013). Alatalo et al. (2013) showed a prominent dusty disk in the $g - r$ image, and a regularly rotating central molecular gas disk in the CO (1 – 0) emission. Onishi et al. (2017) obtained similar results of a prominent dust structure in the *Hubble Space Telescope* (HST) H -band image, and a centrally-concentrated gaseous disk in the CO(2 – 1) observations, and derived the mass of the central super-massive black hole of $5.75 \times 10^8 M_{\odot}$. In Davis et al. (2014), NGC 3665 shows the largest deviation from the so-called Kennicutt-Schmidt relation (Kennicutt 1998a) among 32 CO-detected ATLAS^{3D} ETGs. The abundant cool gas and low SFR surface density (Σ_{SFR}) suggest that NGC 3665 is an atypical ETG. Through studying specific ISM properties, we can better understand its relation to the star formation, especially the reasons for such a low star formation efficiency.

In this paper, we focus on the photometric observations of NGC 3665 at 100, 160, 250, 350 and 500 μm , obtained with the Photodetector Array Camera and Spectrometer (PACS;

Poglitsch et al. 2010) and the Spectral and Photometric Imaging REceiver (SPIRE; Griffin et al. 2010) onboard *Herschel*, with five fine-structure lines of [N II] 122 and 205 μm , [C II] 158 μm , [O I] 63 μm , and [C I] 370 μm . We also perform optical spectroscopic observations of NGC 3665 with the CAHA 3.5m telescope. Using these spectra combined with the analysis of multi-wavelength spectral energy distribution (SED), we investigate SFR, the gas heating and cooling efficiency in PDRs, and the hydrogen nucleus density and the strength of FUV radiation field derived from the PDR models.

This paper is organized as follows. Data reductions for *Herschel* photometric and spectroscopic observations and CAHA 3.5m telescope spectroscopic observations are described in Section 2. We present the results and discuss their implications in Section 3, including the classification of nuclear activity, SED fitting, star formation rate, the ionized gas contribution to the [C II] 158 μm emission, the photoelectric heating efficiency of the interstellar gas, and some derived values using the PDR model. Then, we compare our results with respect to the star formation and gas to the previous works, and discuss the possible mechanisms to suppress star formation in NGC 3665 in Section 4. The conclusions for this work are summarized in Section 5.

2. Observations and Data Reduction

2.1. *Herschel* PACS and SPIRE Photometry

NGC 3665 was observed with *Herschel* PACS and SPIRE in two open time projects GT2_mbaes.2 (PI: M. Baes) and OT1_lyoung.1 (PI: L. Young), respectively. We performed aperture photometry with the public Level 2 map products, which were downloaded from the Herschel Science Archive¹. To match the 36'' resolution of the 500 μm image, we convolved other band images with the kernels provided in Gordon et al. (2008). We adopted the aperture of 40'' radius around the source, and determined the sky values within 60-90'' annulus surrounding the target galaxy. The photometric errors on the source were given by the standard deviation of 15 annulus between 60'' and 90'' around the source, as well as the 5% uncertainty of the fiducial stellar models in the PACS photometry and the confusion noise in the SPIRE photometry (Herschel Observers' Manual², v.5.0.3, 2014). We then applied the corresponding color and aperture corrections to these fluxes. The final photometric fluxes are given in Table 1.

¹http://herschel.esac.esa.int/Science_Archive.shtml

²<http://herschel.esac.esa.int/Docs/Herschel/html/Observatory.html>

2.2. *Herschel* PACS and SPIRE Spectroscopy

The *Herschel* FIR spectroscopic observations of NGC 3665 were performed by the program OT1_lyoung_1 (PI: L. Young; Lapham et al. 2017), with a total exposure time of 60.7 hours of *Herschel*. We focused on the [N II] 122 and 205 μm , [C I] 370 μm , [C II] 158 μm and [O I] 63 μm fine-structure lines observed with the PACS (better than 12'') and SPIRE ($\sim 17''$ and $\sim 36''$) instruments.

2.2.1. PACS flux measurement

The PACS integral-field spectrometer covers the 51-220 μm range with a spectral resolution of $\sim 75\text{--}300 \text{ km s}^{-1}$, which is composed of 5×5 squared spatial pixels (spaxels), each with a size of 9''.4. It covers a total projected field of view (FoV) of $47'' \times 47''$. The angular resolutions are 9''.4 at $\sim 63 \mu\text{m}$, 10''.0 at $\sim 122 \mu\text{m}$, and 11''.5 at $\sim 158 \mu\text{m}$. For NGC 3665, the [O I] 63 μm , [N II] 122 μm and [C II] 158 μm data are comprised of observations acquired in the mapping mode. The Level 2 data with standard rebinned cubes, observed with line range spectroscopy mode and reduced with the Herschel Interactive Processing Environment (HIPE; Ott 2010) version 14.2, were downloaded directly from the Herschel Science Archive. The spectrometer effective spectral resolutions are about 86 km s^{-1} (the third grating order), 290 km s^{-1} (the first grating order) and 238 km s^{-1} (the first grating order) for [O I] 63 μm , [N II] 122 μm and [C II] 158 μm , respectively. The basic observational informations for each line are summarized in Table 2.

Following Farrah et al. (2013), we co-added the spectra of the central 9 spaxels to measure the line fluxes, due to the fact that the line-emitting regions in NGC 3665 are not confined in the central spaxel according to its 100 micron continuum emission. Then we fitted the observed spectrum with two Gaussian functions (for the line) plus a linear component (for the continuum), as shown in Fig. 1. The uncertainty of the integrated flux was calculated according to the rms of the continuum. A point-source aperture correction (Balog et al. 2014) was applied to derive the final flux. The intrinsic line width (σ_{true}) was obtained using $\sigma_{\text{true}} = \sqrt{\sigma_{\text{obs}}^2 - \sigma_{\text{inst}}^2}$, where σ_{obs} and σ_{inst} are the observed line width and instrumental spectral resolution, respectively. The [O I] 63 μm is not detected, and thus we calculated its upper limit using 3σ times the instrumental spectral resolution at the considered wavelength. The line fluxes are given in Table 2. In Fig. 2, we show the [C II] 158 μm and [N II] 122 μm integrated intensity maps, overlaid with the $^{12}\text{CO}(J = 1 - 0)$ moment 0 contours from the CARMA ATLAS^{3D} survey (Alatalo et al. 2013). The maps are created by projecting the rasters onto a common, regular spatial grid with 1.86'' and 1.63'' pixel sizes, respectively, clearly shows that the neutral and ionized gas has extended

structures and follow the CO(1 – 0) gas disk. Both of these two cooling lines are strongest at the center, and weaker outwards, suggesting a mount of [C II] 158 μm lines generate from ionized gas, which emit the [N II] 122 μm . The offset on the nucleus in each panel of [C II] 158 μm and [N II] 122 μm lines compared with CO(1 – 0) contour is smaller than 2'' and within the beam size. Since the non-detection of [O I] 63 μm , and the [N II] 122 μm emission is marginally resolved, we tried but failed to perform radial decomposition. Thus, we only concentrated on the analysis of the integrated properties of NGC 3665.

2.2.2. SPIRE flux measurement

The SPIRE Fourier-Transform Spectrometer (FTS) consists of two bolometer detector arrays, the SPIRE Short Wavelength Spectrometer Array (SSW) and the SPIRE Long Wavelength Spectrometer Array (SLW), covering overlapping bands of 191–318 μm and 294–671 μm , respectively. The observations were conducted in the single pointing mode with a high spectral resolution of 0.04 cm^{-1} (or 1.2 GHz in frequency space). We used the Level 2 data products, which were reduced using the standard pipeline provided by the HIPE version 14.0, along with the SPIRE calibration version 14.2.

To obtain the integrated fluxes of [C I] and [N II] 205 μm lines, we followed the method in Lu et al. (2017). For the [C I] 370 μm line, we adopted a pure *Sinc* function as (1) this line is only partially resolved given the large instrumental resolution ($\sim 540 \text{ km s}^{-1}$) at 370 μm , and (2) the S/N is not high enough to use a Sinc-convolved-Gauss function. For the [N II] 205 μm line, we adopted a Sinc-convolved-Gauss function as the velocity resolution at $\sim 205 \mu\text{m}$ is about 300 km s^{-1} . We also used *FTLinefinder*³ (FTFitter; in version 1.9) to fit the observed spectra, and obtained similar results. Table 2 gives the line fluxes of [N II] 205 μm and [C I] 370 μm .

The SPIRE beam size at 205 μm is $\sim 17''$, and thus might not cover the total emission of the [N II] line. To check this, we used the correlation between the [N II] 205 emission to total infrared luminosity ratio ($L_{[\text{N II}]205 \mu\text{m}}/L_{\text{TIR}}$; see Section 3.2 for the calculation of L_{TIR} used here) and FIR color (Zhao et al. 2016a): $\log(L_{[\text{N II}]205 \mu\text{m}}/L_{\text{TIR}}) = -3.83 - 1.26x - 1.86x^2 - 0.90x^3$, where $x = \log(f_{70}/f_{160})$, and f_{70} and f_{160} represent the flux densities at 70 and 160 μm , respectively. We obtained the total [N II] 205 emission is $\sim 6.12 \times 10^{-17} \text{ W m}^{-2}$, consistent with the measured value within the uncertainties. Furthermore, the [N II] flux is $7.29 \pm 0.14 \times 10^{-17} \text{ W m}^{-2}$ after calibrating with the Semi Extended Correction Tool (SECT) in Lapham et al. (2017). Therefore, the distribution of [N II] 205 μm emission

³<https://www.uleth.ca/phy/naylor/index.php?page=ftfitter>

should not deviate much from a point-like source relative to the $17''$ beam.

2.3. Optical Spectroscopy

The optical spectroscopic observations were carried out with the 3.5-m telescope at Calar Alto Observatory (CAHA⁴, Almería, Spain) on May 26, 2017. We used the PPAK integral-field unit (IFU) (Verheijen et al. 2004) at Potsdam Multi-Aperture Spectrometer (PMAS; Roth et al. 2005) instrument, containing 382 fibers with each of $2.7''$ diameter and a hexagonal FoV of $74'' \times 64''$ (Kelz et al. 2006). The V500 grating, which has a spectral resolution (FWHM) of 6 \AA and wavelength coverage of $3745\text{--}7500 \text{ \AA}$, was adopted. A three-pointing dithering scheme was used with exposure time of 900 seconds each. The typical airmass was ~ 1.1 . Raw spectroscopic data was reduced with the RGB reduction pipeline version 0.0.2, including bias subtraction, flat-field correction, cosmic ray removal, atmospheric extinction correction, as well as wavelength and flux calibration. The wavelength calibration was performed based on Hg/He lamp exposures at the beginning of the observations every time. For the following analysis, we only focus on the central $3'' \times 3''$ (9 spaxels).

To obtain the emission line fluxes, we followed the method of Tremonti et al. (2004) and Brinchmann et al. (2004) to model the stellar continuum with templates, which are generated using the popular synthesis code of Bruzual & Charlot (2003, BC03). The template spectra are composed of ten different ages (0.005, 0.025, 0.1, 0.2, 0.6, 0.9, 1.4, 2.5, 5, 10 Gyr) and four metallicities (0.004, 0.008, 0.017, and 0.05). For each metallicity, we performed a non-negative least square fit to obtain the best-fitting model spectrum using the 10 single-age populations, with the internal dust attenuation model of Charlot & Fall (2000). During the fitting process, each template is convolved with a stellar velocity dispersion from 0 to 200 km s^{-1} by a step size of 5 km s^{-1} . After subtracting the best-fitting stellar continuum model, we obtained the pure nebular emission line spectrum, and fitted each line with one Gaussian component, including $\text{H}\beta$, $\text{H}\alpha$, $[\text{O III}]\lambda 5007$, and $[\text{N II}]\lambda 6584$ lines.

⁴<http://www.caha.es/>

3. Results and Discussion

3.1. Spectral Classification

To identify the power source of the emission lines, we adopted the well-known BPT diagnostic diagram (Baldwin, Phillips & Terlevich 1981; Veilleux & Osterbrock 1987). Here we only focus on the central $3'' \times 3''$ region (the IFU data will be fully used in the following paper for a large sample of S0 galaxies) in NGC 3665. In Fig. 3, we plotted $[\text{N II}]\lambda 6584 / \text{H}\alpha$ versus $[\text{O III}]\lambda 5007 / \text{H}\beta$ flux ratios with $\text{S/N} > 3$ for all of the four emission lines. The red solid and dashed lines mark the criteria to separate AGN from star-forming galaxies according to Kewley et al. (2001) and Kauffmann et al. (2003), respectively, with composite systems located in between these two lines. The horizontal blue line adopted from Kauffmann et al. (2003) is used to divide galaxies into Seyfert and LINERs. Green points represent individual spaxels ($1'' \times 1''$), whereas the red star shows the entire $3'' \times 3''$ region. As shown in Fig. 3, all of the observed points lie in the composite region, suggesting that the central region of NGC 3665 is a mixture of star formation and a weak AGN, and is consistent with Ho et al. (1997).

For the central $3'' \times 3''$ region, the equivalent width of $\text{H}\alpha$ ($W_{\text{H}\alpha}$) is $\sim 3.82 \text{ \AA}$, and $\log([\text{N II}]/\text{H}\alpha)$ is about -0.21, which are also consistent with the identification of weak AGN (i.e., $\log([\text{N II}]/\text{H}\alpha) > -0.4$ and $W_{\text{H}\alpha}$ between 3 and 6 \AA) in the $W_{\text{H}\alpha}$ versus $[\text{N II}]/\text{H}\alpha$ (WHAN) diagram (Cid Fernandes et al. 2011). Our results are consistent with Nyland et al. (2016), who detected two extended radio jets on scale of kilo parsecs in NGC 3665.

Using the observed ratio of $F_{\text{H}\alpha}/F_{\text{H}\beta}$, we can estimate the nebular extinction, $A_{V,\text{nebular}}$ (Cardelli et al. 1989), assuming an unreddened $I_{\text{H}\alpha}/I_{\text{H}\beta}$ of 2.86 from Osterbrock (1989), e.g.,

$$A_{V,\text{nebular}} = 7.2 \times \log \left(\frac{F_{\text{H}\alpha}/F_{\text{H}\beta}}{I_{\text{H}\alpha}/I_{\text{H}\beta}} \right). \quad (1)$$

We obtained that the nebular extinction, $A_{V,\text{nebular}}$, for NGC 3665 is ~ 1.3 , which is larger than the mean value, 1.06 ± 0.66 , of 45 star-forming S0 galaxies (Xiao et al. 2016) from the Sloan Digital Sky Survey (SDSS; Abazajian et al. 2009).

Here we roughly calculate the surface density of star formation rate in the central $3'' \times 3''$ region, Σ_{SFR} , without considering the effect of weak AGN. Using Kennicutt (1998b) relation with extinction-corrected H_α luminosity:

$$\text{SFR} (M_\odot \text{ yr}^{-1}) = 7.9 \times 10^{-42} L(H_\alpha) (\text{ergs s}^{-1}), \quad (2)$$

we derive $\log \Sigma_{\text{SFR}} \sim -0.78 M_\odot \text{ yr}^{-1} \text{ kpc}^{-2}$, which is lower than the mean value, $-0.48 M_\odot \text{ yr}^{-1} \text{ kpc}^{-2}$, of 45 star-forming S0 galaxies with the same method (Xiao et al. 2016).

Since the [N II] 122 μm emission is the strongest in the center (see Fig. 2), suggesting a similar distribution of H II regions (Zhao et al. 2016a), we conclude that the star formation is concentrated in the galactic center and the rate is low.

3.2. SED Fitting

To better understand the infrared properties of NGC 3665, such as the total infrared luminosity (L_{TIR} ; 8-1000 μm as defined in Sanders & Mirabel 1996), dust temperature (T_{dust}) and dust mass (M_{dust}), we used the code of Multi-wavelength Analysis of Galaxy Physical Properties⁵ (MAGPHYS; da Cunha et al. 2008) to fit the observed SED of NGC 3665. Besides the *Herschel* PACS and SPIRE photometric results, we also compiled UV to FIR photometries from Galaxy Evolution Explorer (*GALEX*; Loubser & Sánchez-Blázquez 2011), SDSS (Adelman-McCarthy et al. 2008), Two Micron All Sky Survey (2MASS; Jarrett et al. 2000), and Infrared Astronomical Satellite (*IRAS*; Moshir et al. 1990) catalogs. The measured fluxes are listed in Table 3.

MAGPHYS is a simple model to interpret in a consistent way the emission from galaxies at UV, optical and IR wavelengths in terms of their star formation histories and dust content, using a Bayesian fitting method. The library of model galaxy spectra are composed of two types of binary files: the ‘optical models’ tracing the emission from stellar populations in galaxies, calculated using BC03 with initial mass function (IMF) from Chabrier (2003) and the dust attenuation model described in Charlot & Fall (2000); the ‘infrared models’ tracing the emission from dust, following the approach described in da Cunha et al. (2008). This model relies on the assumption that the total energy absorbed by dust from two main components (Charlot & Fall 2000): the stellar birth clouds (star-forming regions) and the ambient diffuse ISM, and re-radiated by dust at IR wavelengths via an energy balance argument.

We present the result of SED fitting for NGC 3665 in Fig. 4. In the top panel, the black line shows the best model fitting to the observed data (red points), the blue and red lines represent the unattenuated stellar population spectrum and the dust emission, respectively. The residuals $(L_{\text{obs}} - L_{\text{mod}})/L_{\text{obs}}$ are shown with black squares. As we can see that the modeled spectrum is in good agreement with the observed data points from *GALEX* 1539 Å to *Herschel* SPIRE 500 μm .

Table 4 lists the derived parameters from the best-fit SED. The dust to stellar mass

⁵<http://www.iap.fr/magphys/magphys/MAGPHYS.html>

ratio M_{dust}/M_* of NGC 3665 is about 1.1×10^{-4} , which is about 3 times higher than the mean value for 39 S0+S0a galaxies observed with *Herschel* (Smith et al. 2012). As shown in Alatalo et al. (2013), NGC 3665 has a total molecular gas mass of $\log M_{\text{gas}} = 9.11 \pm 0.01 M_{\odot}$, indicating that the gas-to-dust mass ratio (GDR) is ~ 182 , which is similar to the value of the Milky Way, e.g., ~ 120 from Li & Draine (2001), ~ 160 from Zubko et al. (2004), and ~ 180 from Draine et al. (2007). We also calculated the total infrared luminosity (L_{IR}) of NGC 3665, integrated within 8-1000 μm from SED best-fitting model, to be $10^{9.88 \pm 0.02} L_{\odot}$. The error is estimated through performing a Monte Carlo simulation, sampling a series of data points according to a Gaussian distribution with the measured photometric values and errors, and repeated the same fitting procedure for 1,000 times using the simulated datasets.

We also ran another SED fitting model CIGALE⁶ (Noll et al. 2009) version 0.11.0 to make a comparison. The derived values of stellar mass and dust luminosity are $\log M_* = 10.79 M_{\odot}$ and $\log L_{\text{d}} = 9.97 L_{\odot}$, respectively, consistent with the results from MAGPHYS. Therefore, we adopted the fitted parameters from MAGPHYS in the following analysis.

3.3. Star Formation Rate

To estimate the star formation rate (SFR) in NGC 3665, we adopted several different approaches:

- (1) Using the infrared and *GALEX* far-UV luminosity (Dale et al. 2007):

$$\text{SFR} (M_{\odot} \text{yr}^{-1}) = 4.5 \times 10^{-37} L_{\text{TIR}} (\text{W}) + 7.1 \times 10^{-37} \nu L_{\nu} (1500 \text{ \AA}) (\text{W}), \quad (3)$$

where L_{TIR} is calculated from integration within 8-1000 μm from SED fitting (see the Section 3.2). The SFR in NGC 3665 is derived to be $1.34 \pm 0.06 M_{\odot} \text{yr}^{-1}$.

- (2) Based only on L_{TIR} , with the algorithm of Kennicutt (1998b):

$$\text{SFR} (M_{\odot} \text{yr}^{-1}) = 4.5 \times 10^{-44} L_{\text{TIR}} (\text{ergs s}^{-1}). \quad (4)$$

The derived SFR is $1.29 \pm 0.06 M_{\odot} \text{yr}^{-1}$. As we know, the weak AGN in NGC 3665 might contribute to the IR emission, which leads to an overestimated SFR. However, the results of CIGALE suggest that the fractional contribution of AGN to the dust emission, f_{AGN} , is less than 0.01, thus we ignored its contribution to the infrared luminosity.

- (3) As shown in Zhao et al. (2013, 2016a), the [N II] 205 μm luminosity ($L_{[\text{N II}]205 \mu\text{m}}$) is less affected by emissions from older stars compared to the IR luminosity, it is also a good

⁶<http://cigale.lam.fr>

indicator of SFR. With the 60-to-100 μm flux density ratio, $f_{60}/f_{100} \sim 0.3$ in NGC 3665, we adopted the relation suitable for the cold FIR color ($0.2 \leq f_{60}/f_{100} < 0.6$):

$$\log \text{SFR} (M_{\odot} \text{yr}^{-1}) = -5.99 + \log L_{[\text{N II}]} (L_{\odot}). \quad (5)$$

We calculated SFR to be $2.55^{+1.68}_{-1.01} M_{\odot} \text{yr}^{-1}$, where the error is estimated from the uncertainty (0.22 dex) associated with the SFR calibrator given in Zhao et al. (2016a).

(4) The [C II] 158 μm emission can also be served as a useful indicator of SFR (Sargsyan et al. 2014), as:

$$\log \text{SFR} (M_{\odot} \text{yr}^{-1}) = \log L_{[\text{C II}]} (L_{\odot}) - 7.0, \quad (6)$$

with a scatter of 0.2 dex. The derived SFR is $1.66^{+0.61}_{-0.97} M_{\odot} \text{yr}^{-1}$.

Therefore, SFRs from different calibrators are consistent with each other within uncertainties, and we take the averaged value of $1.7 M_{\odot} \text{yr}^{-1}$ as the final result.

3.4. The Photodissociation Region

3.4.1. [C II] Emission from Ionized Gas

The emission of [C II] originates from both the neutral and ionized gas, due to the low ionization potential (11.26 eV) of atomic carbon. To use the PDR models, in which only the emission from neutral gas has been taken into account, we first need to remove the [C II] emission from ionized gas. Following the method of Oberst et al. (2006, 2011), the contribution of ionized gas can be estimated with the [C II]/[N II] 205 ratio, which is only a function of electron density (n_e) in the H II regions after assuming a C/N abundance ratio. n_e can be estimated with the [N II] 122/[N II] 205 ratio because of their different critical densities (Oberst et al. 2006; Zhao et al. 2016a). Compared the observed value (1.95 ± 0.27) with the theoretical curve, we determine $n_e = 49.5 \pm 11.9 \text{ cm}^{-3}$, which is comparable to those found in ETGs and star-forming galaxies. For instance, Lapham et al. (2017) found $n_e = 24 \text{ cm}^{-3}$ for 11 nearby ETGs from *Herschel* observations, and Díaz-Santos et al. (2017) found n_e from 20 to 100 cm^{-3} , with the mean value of 45 cm^{-3} , for 240 GOALS luminous IR galaxies (LIRGs). In the Milky Way, the average value is measured to be 29 cm^{-3} (Goldsmith et al. 2015), and in nearby spiral galaxy NGC 891, n_e is ranging from 1.9 to 80 cm^{-3} , with a mean value of 22 cm^{-3} (Hughes et al. 2015).

Based on the Lick indices (Fe5015 and Mg *b*) and single stellar population models, McDermid et al. (2015) derived the stellar metallicity at $R_e/8$ ($\sim 0.87 \text{ kpc}$) to be $[\text{Z}/\text{H}] = -0.05 \pm 0.05$. We calculated gas-phase metallicity based on the [N II] λ 6584/H α line ratio

(Kewley & Dopita 2002) for the same central region, to be $\sim 1.0 Z_{\odot}$. Thus, by adopting a solar abundances of $C/H = 1.4 \times 10^{-4}$ and $N/H = 7.9 \times 10^{-5}$ from Savage & Sembach (1996), we further used the derived electron density to predict the $[C\ II]/[N\ II]$ 205 ratio in ionized gas, and then compared it with the observed values. We find that the fraction of $[C\ II]$ emission from ionized gas is about 43%. This value appears consistent with the previous results from various sources that the majority of $[C\ II]$ emission comes from PDRs (Abel et al. 2005; Oberst et al. 2006, 2011; Farrah et al. 2013; Parkin et al. 2014; Hughes et al. 2015; Lapham et al. 2017). After removing contribution from ionized gas for the $[C\ II]$ emission, we estimated the $[C\ II]$ flux originating from neutral gas is $(27.6 \pm 0.5) \times 10^{-17} \text{ W m}^{-2}$.

3.4.2. Gas Heating and Cooling

The $[C\ II]$ 158 μm and $[O\ I]$ 63 μm are dominant coolants in neutral gas of PDRs, which can help us constrain the physical conditions of neutral ISM. The strengths of these two lines show how many interstellar UV photons heat the gas by photoelectric effect, which can be traced by emission lines during gas cooling via collisional excitation at the FIR wavelengths. Another proportion of UV photons are absorbed by dust grains, and re-emit in the infrared, which can be traced by total infrared flux. Therefore, the ratio of $([C\ II]+[O\ I]63)/F_{\text{TIR}}$ is a criterion for diagnosing photoelectric heating efficiency of the interstellar gas (Tielens & Hollenbach 1985).

The total infrared flux, F_{TIR} , is $2.19 \times 10^{-13} \text{ W m}^{-2}$, we calculated the $([C\ II]+[O\ I]63)/F_{\text{TIR}}$ ratio in PDRs to be in the range of 1.26×10^{-3} and 1.37×10^{-3} , where the lower and upper limits were obtained by assuming zero and 3σ fluxes of the $[O\ I]$ emission, respectively. Whereas the typical values of $([C\ II]+[O\ I]63)/F_{\text{TIR}}$ are in the range of 10^{-3} to 10^{-2} , both in ETGs and late-type galaxies (Malhotra et al. 2001; Brauher et al. 2008; Lapham et al. 2017). For other galaxies with spatially resolved observations, the heating efficiency varies between $\sim 2 \times 10^{-3}$ and 10^{-2} in the late spiral galaxy NGC 1097 and Seyfert 1 galaxy NGC 4559 (Croxall et al. 2012). Hughes et al. (2015) also found in NGC 891, the $([C\ II]+[O\ I]63)/F_{\text{TIR}}$ ranging from $\sim 1 \times 10^{-3}$ to 2×10^{-2} using *Herschel* FIR spectroscopic observations. Parkin et al. (2014) showed that the heating efficiency in the disk of Centaurus A is ranging from 4×10^{-3} to 8×10^{-3} . In the arm and inter-arm regions of M51, the average value is up to $\sim 10^{-2}$, and in the nucleus decreasing to 3×10^{-3} (Parkin et al. 2013). Therefore, NGC 3665 is among those sources having the lowest gas heating efficiency.

The low gas heating efficiency in NGC 3665 might be caused by its weak UV radiation field. The gas is mainly photoelectrically heated by the UV photons, while dust can be

heated by both optical and UV photons (Malhotra et al. 2000). As shown in Abel et al. (2009), the FIR color is a good indicator of the ionization parameter (U) of the ambient UV radiation field. For NGC 3665, $f_{60}/f_{100} \sim 0.3$ indicates a very small U of $\sim 10^{-4}$. Therefore, there is not enough energy for the electron to collisionally excited the C^+ and O to higher levels.

3.4.3. The PDR Model

We compare IR emission line ratios to PDR model to obtain the physical properties of the PDR regions. Here we adopt the PDR model of Kaufman et al. (1999, 2006), which has been updated based on the original model of Tielens & Hollenbach (1985). These models assume a homogeneous semi-infinite two-dimensional slab of a PDR and solve for the chemistry, thermal balance, and radiation transfer simultaneously. For given gas-phase elemental abundances and grain properties, the model is parameterized by two free parameters: the hydrogen nucleus density, n , and the strength of FUV ($6 \text{ eV} < E < 13.6 \text{ eV}$) radiation field, G_0 , in units of $1.6 \times 10^{-3} \text{ erg cm}^{-2} \text{ s}^{-1}$ from the local Galactic interstellar FUV field (Habing 1968).

We adopt the diagnostic observed line ratios of $[C \text{ II}]/[O \text{ I}]63$ versus $([C \text{ II}]+[O \text{ I}]63)/F_{\text{TIR}}$ as mentioned in Wolfire et al. (1990). Here we make several corrections to the observed quantities following the strategy of Zhao et al. (2016b). The cloud is optically thin to the infrared continuum photon, which contributes to the actual observations from the front and back side of the cloud (especially when they are illuminated from all sides), while the models only take into account one side emission exposed to the source of UV photons. Therefore, we reduce the observed F_{TIR} by a factor of 2 as suggested by Kaufman et al. (1999).

In the PDR models, the emission line is only considered to originate from neutral gas. As mentioned above, the $[C \text{ II}]$ emission arises from both neutral and ionized gas, we first need to remove the contribution of $[C \text{ II}]$ from ionized gas, with the fraction of $\sim 43\%$. Besides, we correct the geometrical effect of PDR models to the observed $[C \text{ II}]$ emission. The $[C \text{ II}]$ is marginally optically thick with optical depth $\tau \sim 1$ at the line center (Kaufman et al. 1999), thus the observed emission comes from the front side and partial back side of the cloud. We adopt the correction factor of 1.4 to divide the observed flux when comparing to the two-dimensional PDR models. More methodology details are described in Zhao et al. (2016b). The $[O \text{ I}]63$ line is optically thick. We observe the emission only from the front side of the cloud, while the other about half of the total $[O \text{ I}]63$ emission radiates away from the line of sight. Accordingly, the actual observed $[O \text{ I}]63$ flux follows the geometrical assumption of PDR models, without any correction applied. Finally, the equation of $([C \text{ II}]+[O \text{ I}]63)/F_{\text{TIR}}$

after correcting is listed in here: $([\text{C II}]/1.4 + [\text{O I}]\lambda 63)/(F_{\text{TIR}}/2.0)$, where the $[\text{C II}]$ emission is only taken into account originating from neutral gas.

Through a comparison of two observed line ratios to the two-dimensional PDR model, with χ^2 minimization in the web-based Photo Dissociation Region Toolbox (PDRT; Pound & Wolfire 2008)⁷, the derived values of hydrogen volume density, n , and the incident FUV radiation field, G_0 , are listed in Table 5. We also list the best-fitting results derived from uncorrected diagnostic observed line ratios in the PDR region compared to the model. Meanwhile, both results before and after correction are shown in Fig. 5. The G_0 in NGC 3665 is significantly lower than what found in normal, star-forming, and starburst galaxies, and galaxies with strong AGN (Negishi et al. 2001; Malhotra et al. 2001; Kramer et al. 2005; Oberst et al. 2011; Croxall et al. 2012; Parkin et al. 2013; Zhao et al. 2016b). The low G_0 indicates a weak FUV radiation field, which is consistent with our previous analysis.

F_{TIR} is calculated among the whole galaxy, while $[\text{C II}]$ emission tend to concentrate in the center of NGC 3665 (see the Fig. 2) as well as the $[\text{O I}]\lambda 63$ emission, which might result in the low G_0 after comparing with the PDR model. Here we focus on the central spaxel, with a size of $9''.4 \times 9''.4$, to discuss the physical properties of ISM. The $[\text{C II}]$ and $[\text{O I}]\lambda 63$ line fluxes in the central region are measured using the same method as in Section 2.2.1. We calculate the central infrared luminosity of NGC 3665 using *Herschel* photometry at 100, 160 and 250 μm , following Galametz et al. (2013):

$$L_{\text{TIR}} (L_{\odot}) = (1.379 \pm 0.025)L_{100\mu\text{m}} + (0.058 \pm 0.049)L_{160\mu\text{m}} + (1.150 \pm 0.092)L_{250\mu\text{m}}, \quad (7)$$

where $L_{100\mu\text{m}}$, $L_{160\mu\text{m}}$ and $L_{250\mu\text{m}}$ are band luminosities in the unit of L_{\odot} . The central infrared luminosity is estimated to be $(49.5 \pm 2.3) \times 10^7 L_{\odot}$. After comparing the two observed line ratios to the PDR model, we derive two physical parameters in the central PDRs of NGC 3665: the hydrogen nucleus density, $n \sim 5.62 \times 10^3 \text{ cm}^{-3}$, and the strength of FUV radiation field, $G_0 \sim 10^{0.25}$. The G_0 in the central region of NGC 3665 is about 3 times larger than that derived from the whole galaxy, while this value is still low enough to indicate a weak FUV radiation field.

4. Abundant Molecular Gas and Suppressed Star Formation

Comparing with the so-called ‘star-forming main sequence’ (stellar mass-SFR relation) at $z \sim 0$ (Elbaz et al. 2007), NGC 3665 lies 0.5 dex lower than the locus of star-forming galaxies

⁷<http://dustem.astro.umd.edu/pdrt/>

at the fixed stellar mass, showing that star formation is suppressed. In Davis et al. (2014), NGC 3665 has $\log \Sigma_{\text{SFR}}$ down to $-2.15 M_{\odot} \text{ yr}^{-1} \text{ kpc}^{-2}$, and shows the largest deviation from the Kennicutt-Schmidt (KS) relation among 32 CO-detected ATLAS^{3D} ETGs. The gas (atomic+molecular) surface density (Σ_{gas}) of NGC 3665 is ~ 0.9 dex larger than that of spiral galaxies at the same Σ_{SFR} . Furthermore, its molecular gas surface density ($2.16 M_{\odot} \text{ pc}^{-2}$; Davis et al. 2014) is significant larger than spiral galaxies at a given Σ_{SFR} in the KS plane (Bigiel et al. 2008; Leroy et al. 2008, 2013). Shi et al. (2011, 2018) proposed an extended Schmidt law, invoking the stellar mass to be a secondary role (the first is gas mass) in regulating star formation, as $\Sigma_{\text{SFR}} \propto (\Sigma_{\text{star}}^{0.5} \Sigma_{\text{gas}})^{1.09}$. We also compared NGC 3665 with the extended Schmidt law, and found that it has the largest offset to this relation among 20 ETGs, and has $\Sigma_{\text{star}}^{0.5} \Sigma_{\text{gas}} \sim 1.6$ dex larger than late-type galaxies at the same Σ_{SFR} . Here we have calculated the stellar mass surface density to be $\log \Sigma_{\text{star}} = 3.56 M_{\odot} \text{ pc}^{-2}$ with the same method mentioned in the following as Fang et al. (2013). These results reveal that NGC 3665 has large gas reservoirs while less star formation.

Meanwhile, NGC 3665 is in a low density environment, with the local galaxy surface density within the radius to the 10th nearest neighbor of $\log \Sigma_{10} = -1.24 Mpc^{-2}$, and has been classified into field galaxy in Cappellari et al. (2011). Young et al. (2011) further explained that the poor environment might induce in large CO storage in galaxies by cool gas accretion. We derived the contribution from cold dust to the total dust luminosity ($\xi_{\text{C}}^{\text{tot}}$) to be ~ 70 per cent from MAGPHYS, and calculate $f_{60}/f_{100} \sim 0.3$ to classify NGC 3665 into ‘cold’ galaxy as Zhao et al. (2016a). These results reveal a high cool gas proportion in our source. Among current studies, scenarios proposed to prevent star formation can be roughly divided into three different routines: the cutoff of gas inflow, the removal (or heat) of cool gas in galaxies, and the stabilization of cold gas reservoirs (Martig et al. 2009; Fang et al. 2013; Bluck et al. 2014).

We carried out a two-dimensional (2D) bulge-disk decomposition using GALFIT (version 3.0.5; Peng et al. 2002, 2010), and find that the SDSS (Gunn et al. 1998; Aihara et al. 2011) r -band image of NGC 3665 can be fitted very well with one Sérsic component. The fitting results are listed in Table 6, and shown in Fig. 6. The Sérsic index is 3.81, showing that NGC 3665 is a typical bulge-dominated galaxy. Fang et al. (2013) found the stellar mass surface density within 1 kpc, Σ_1 , is a critical indicator of the star formation suppression. We calculate Σ_1 following Fang’s method. Using the relation between stellar mass-to- i -band luminosity ratio and rest-frame $g-i$ color, $\log M/L_i = 1.15 + 0.79 (g - i)$, we measure the value of $\log \Sigma_1$ to be $\sim 9.79 M_{\odot} \text{ kpc}^{-2}$. This value is about 0.15 dex higher than the best-fit Σ_1 vs. stellar mass relation for green valley and red sequence galaxies at the fixed stellar mass (Figure 4 in Fang et al. 2013), indicating a relatively compact spheroidal stellar component in our source. With such a compact, massive bulge to stabilize cold gas reservoirs, star

formation can be suppressed effectively in NGC 3665.

On the other hand, we estimate the Toomre Q parameter to explore whether the molecular gas disk is stable enough to against the gravitational fragmentation, following the criteria of Toomre (1964):

$$Q_{\text{gas}} = \frac{\sigma_{\text{gas}} \kappa}{\pi G \Sigma_{\text{gas}}} > 1. \quad (8)$$

σ_{gas} is the molecular gas velocity dispersion to be 12.53 km s^{-1} with the CARMA observations (Onishi et al. 2017), κ is the epicyclic frequency adopted of a approximate relation $\kappa \sim \sqrt{2} V(R)/R$, G is Newton’s gravitational constant, and Σ_{gas} is the surface density of the gas disk to be $\sim 145 M_{\odot} \text{ pc}^{-2}$. Thus we derive $Q_{\text{gas}} \sim 2.6$, suggesting a stable molecular gas disk to against large-scale gas self-gravitational collapse.

Besides the effect of a massive bulge, this galaxy has two extended jets on kilo parsec scales (Nyland et al. 2016), which can both heat the halo gas and expel a fraction of the cool gas (AGN ‘radio-mode’ feedback; Croton et al. 2006; Ogle et al. 2007; Nesvadba et al. 2010; Lanz et al. 2016; Smethurst et al. 2016; Combes 2017). In addition, on account of the high stellar mass of $10.79 M_{\odot}$, there is another possible mechanism to prevent star formation by shock heating the gas inflow from the halo (Kereš et al. 2005; Dekel & Birnboim 2006; Cappellari 2016). However, with the low percentage of hot gas, these two modes of star formation suppression are unlikely the dominant mechanisms in NGC 3665. The metallicity is $\sim 1.0 Z_{\odot}$, thus we can exclude the effect of the metallicity in lowing star formation (Shi et al. 2014).

Consequently, the suppression of star formation in NGC 3665 is most possibly caused by its compact, massive bulge through stabilizing cold gas, which enables NGC 3665 to serve as a good observational sample for the stabilization of cold gas reservoirs, and is influenced by the ‘radio-mode’ feedback as well as the virial shocks. The low rate of star formation and weak AGN produce a weak UV radiation field (shown details in section 3.4.3), thus more dust is heated by old stars with inefficient photoelectric heating of the gas. The weak UV radiation field can not produce much [C II] and [O I]63 emission and lead to somewhat low $([\text{C II}] + [\text{O I}]63)/F_{\text{TIR}}$ in this atypical early-type galaxy.

5. Conclusions

We present *Herschel* FIR photometric and spectroscopic observations of NGC 3665. To better understand the nuclear activity in NGC 3665, we also conducted optical spectroscopic observations. By combining the multi-wavelength data from literature and fitting the observed SED, we obtain dust luminosity, stellar and dust mass, dust temperature, infrared

luminosity, and gas-to-dust mass ratio in NGC 3665. We discuss gas heating and cooling efficiency in the PDR regions and compare observed emission line ratios to the Kaufman et al. (1999, 2006) PDR models to derive hydrogen nucleus density and strength of FUV radiation field. The main results are summarized as follows:

1. From the PACS spectroscopic maps of [C II] 158 μm and [N II] 122 μm , we find that both neutral and ionized gas have extend structures and follow the CO(1 – 0) gas disk distribution. The fluxes are strongest at the center, and gradually weaker outwards.
2. NGC 3665 has dust-to-stellar mass ratio $M_{\text{dust}}/M_* \sim 1.1 \times 10^{-4}$, which is nearly 3 times larger than the mean value of local S0+S0a galaxies. The gas-to-dust mass ratio is 182, similar to that in the Milky Way, indicating a large gas reservoir.
3. According to the BPT diagnostic diagram, NGC 3665 contains both star formation and a weak AGN in the central region. We calculated the SFR to be around $1.7 M_{\odot} \text{ yr}^{-1}$ based on several different methods.
4. The electron density of ionized gas in NGC 3665, based on the [N II] 122/[N II] 205 ratio, is $n_e = 49.5 \pm 11.9 \text{ cm}^{-3}$. The contribution of ionized gas region to the total [C II] emission is about 43%, which is consistent with the previous results that the majority of [C II] emission comes from PDRs.
5. The $([\text{C II}]+[\text{O I}63])/F_{\text{TIR}}$ line ratio is in the range of 1.26×10^{-3} and 1.37×10^{-3} , indicating that NGC 3665 almost has the lowest gas heating efficiency in PDRs among different kinds of galaxies.
6. A comparison between the observed emission line ratios and the theoretical PDR models gives that the hydrogen nucleus density $n \sim 10^{3.75} \text{ cm}^{-3}$, and the strength of FUV radiation field $G_0 \sim 10^{-0.25}$, indicating a very weak UV radiation field in NGC 3665.
7. After comparing our results with previous works, we find that NGC 3665 has large gas reservoirs while low-level star formation. The suppressed star formation is most possibly caused by its compact, massive bulge through stabilizing cool gas reservoirs.

Acknowledgments

The authors are very grateful to the anonymous referee for critical comments and instructive suggestions, which significantly strengthened the analyses in this work. We thank Dr. Daizhong Liu and Dr. Zhiyu Zhang for helpful guidances about data reductions for

Herschel photometric and spectroscopic observations, thank Peng Wei for running SED fitting model CIGALE to help us compare the results with those in model MAGPHYS, and thank David Elbaz, Yifei Jin and Longji Bing for valuable discussions and advices which improved this paper. We are grateful to Sebastián Sánchez, resident astronomer at CAHA, for the optical spectroscopic observations and Rubén García Benito for his help of data reduction. This work is supported by the National Key Research and Development Program of China (No. 2017YFA0402703 and 2017YFA0402704), and by the National Natural Science Foundation of China (Nos. 11673057 and 11733002).

PACS has been developed by a consortium of institutes led by MPE (Germany) and including UVIE (Austria); KU Leuven, CSL, IMEC (Belgium); CEA, LAM (France); MPIA (Germany); INAF-IFSI/OAA/OAP/OAT, LENS, SISSA (Italy); IAC (Spain). This development has been supported by the funding agencies BMVIT (Austria), ESA-PRODEX (Belgium), CEA/CNES (France), DLR (Germany), ASI/INAF (Italy), and CICYT/MCYT (Spain). SPIRE has been developed by a consortium of institutes led by Cardiff University (UK) and including Univ. Lethbridge (Canada); NAOC (China); CEA, LAM (France); IFSI, Univ. Padua (Italy); IAC (Spain); Stockholm Observatory (Sweden); Imperial College London, RAL, UCL-MSSL, UKATC, Univ. Sussex (UK); and Caltech, JPL, NHSC, Univ. Colorado (USA). This development has been supported by national funding agencies: CSA (Canada); NAOC (China); CEA, CNES, CNRS (France); ASI (Italy); MCINN (Spain); SNSB (Sweden); STFC and UKSA (UK); and NASA (USA). HIPE is a joint development by the Herschel Science Ground Segment Consortium, consisting of ESA, the NASA Herschel Science Center, and the HIFI, PACS and SPIRE consortia. Based on observations collected at the Centro Astronómico Hispano Alemán (CAHA) at Calar Alto, operated jointly by the Max-Planck Institut für Astronomie and the Instituto de Astrofísica de Andalucía (CSIC).

REFERENCES

- Abazajian, K. N., Adelman-McCarthy, J. K., Agüeros, M. A., et al. 2009, *ApJS*, 182, 543
- Abel, N. P., Ferland, G. J., Shaw, G., & van Hoof, P. A. M. 2005, *ApJS*, 161, 65
- Abel, N. P., Dudley, C., Fischer, J., Satyapal, S., & van Hoof, P. A. M. 2009, *ApJ*, 701, 1147
- Adelman-McCarthy, J. K., Agüeros, M. A., Allam, S. S., et al. 2008, *ApJS*, 175, 297-313
- Aihara, H., Allende Prieto, C., An, D., et al. 2011, *ApJS*, 193, 29
- Alatalo, K., Davis, T. A., Bureau, M., et al. 2013, *MNRAS*, 432, 1796

- Baldwin, J. A., Phillips, M. M., & Terlevich, R. 1981, *PASP*, 93, 5
- Balog, Z., Müller, T., Nielbock, M., et al. 2014, *Experimental Astronomy*, 37, 129
- Bigiel, F., Leroy, A., Walter, F., et al. 2008, *AJ*, 136, 2846
- Birnboim, Y., & Dekel, A. 2003, *MNRAS*, 345, 349
- Bluck, A. F. L., Mendel, J. T., Ellison, S. L., et al. 2014, *MNRAS*, 441, 599
- Brauher, J. R., Dale, D. A., & Helou, G. 2008, *ApJS*, 178, 280-301
- Brinchmann, J., Charlot, S., White, S. D. M., et al. 2004, *MNRAS*, 351, 1151
- Bruzual, G., & Charlot, S. 2003, *MNRAS*, 344, 1000
- Cappellari, M., Emsellem, E., Krajnović, D., et al. 2011, *MNRAS*, 413, 813
- Cappellari, M. 2016, *ARA&A*, 54, 597
- Cardelli, J. A., Clayton, G. C., & Mathis, J. S. 1989, *ApJ*, 345, 245
- Chabrier, G. 2003, *PASP*, 115, 763
- Charlot, S., & Fall, S. M. 2000, *ApJ*, 539, 718
- Cid Fernandes, R., Stasińska, G., Mateus, A., & Vale Asari, N. 2011, *MNRAS*, 413, 1687
- Combes, F. 2017, *Frontiers in Astronomy and Space Sciences*, 4, 10
- Croton, D. J., Springel, V., White, S. D. M., et al. 2006, *MNRAS*, 365, 11
- Croxall, K. V., Smith, J. D., Wolfire, M. G., et al. 2012, *ApJ*, 747, 81
- da Cunha, E., Charlot, S., & Elbaz, D. 2008, *MNRAS*, 388, 1595
- Dale, D. A., Gil de Paz, A., Gordon, K. D., et al. 2007, *ApJ*, 655, 863
- Davis, T. A., Alatalo, K., Bureau, M., et al. 2013, *MNRAS*, 429, 534
- Davis, T. A., Young, L. M., Crocker, A. F., et al. 2014, *MNRAS*, 444, 3427
- de Vaucouleurs, G., de Vaucouleurs, A., Corwin, H. G., Jr., et al. 1991, *Third Reference Catalogue of Bright Galaxies. Vol. I, Vol. II, Vol. III* (New York: Springer), 2091
- Dekel, A., & Birnboim, Y. 2006, *MNRAS*, 368, 2

- Di Matteo, T., Springel, V., & Hernquist, L. 2005, *Nature*, 433, 604
- Díaz-Santos, T., Armus, L., Charmandaris, V., et al. 2013, *ApJ*, 774, 68
- Díaz-Santos, T., Armus, L., Charmandaris, V., et al. 2017, *arXiv:1705.04326*
- Draine, B. T., Dale, D. A., Bendo, G., et al. 2007, *ApJ*, 663, 866
- Elbaz, D., Daddi, E., Le Borgne, D., et al. 2007, *A&A*, 468, 33
- Fang, J. J., Faber, S. M., Koo, D. C., & Dekel, A. 2013, *ApJ*, 776, 63
- Farrah, D., Leboutteiller, V., Spoon, H. W. W., et al. 2013, *ApJ*, 776, 38
- Galametz, M., Kennicutt, R. C., Calzetti, D., et al. 2013, *MNRAS*, 431, 1956
- Goldsmith, P. F., Yıldız, U. A., Langer, W. D., & Pineda, J. L. 2015, *ApJ*, 814, 133
- Gordon, K. D., Engelbracht, C. W., Rieke, G. H., et al. 2008, *ApJ*, 682, 336-354
- Griffin, M. J., Abergel, A., Abreu, A., et al. 2010, *A&A*, 518, L3
- Gunn, J. E., Carr, M., Rockosi, C., et al. 1998, *AJ*, 116, 3040
- Habing, H. J. 1968, *Bull. Astron. Inst. Netherlands*, 19, 421
- Ho, L. C., Filippenko, A. V., & Sargent, W. L. W. 1997, *ApJS*, 112, 315
- Hopkins, P. F., Hernquist, L., Cox, T. J., et al. 2006, *ApJS*, 163, 1
- Hughes, T. M., Foyle, K., Schirm, M. R. P., et al. 2015, *A&A*, 575, A17
- Jarrett, T. H., Chester, T., Cutri, R., et al. 2000, *AJ*, 119, 2498
- Kamenetzky, J., Rangwala, N., Glenn, J., Maloney, P. R., & Conley, A. 2016, *ApJ*, 829, 93
- Kaufman, M. J., Wolfire, M. G., Hollenbach, D. J., & Luhman, M. L. 1999, *ApJ*, 527, 795
- Kauffmann, G., Heckman, T. M., Tremonti, C., et al. 2003, *MNRAS*, 346, 1055
- Kaufman, M. J., Wolfire, M. G., & Hollenbach, D. J. 2006, *ApJ*, 644, 283
- Kelz, A., Verheijen, M. A. W., Roth, M. M., et al. 2006, *PASP*, 118, 129
- Kennicutt, R. C., Jr. 1998a, *ApJ*, 498, 541
- Kennicutt, R. C., Jr. 1998b, *ARA&A*, 36, 189

- Kereš, D., Katz, N., Weinberg, D. H., & Davé, R. 2005, *MNRAS*, 363, 2
- Kewley, L. J., Dopita, M. A., Sutherland, R. S., Heisler, C. A., & Trevena, J. 2001, *ApJ*, 556, 121
- Kewley, L. J., & Dopita, M. A. 2002, *ApJS*, 142, 35
- Krajnović, D., Emsellem, E., Cappellari, M., et al. 2011, *MNRAS*, 414, 2923
- Kramer, C., Mookerjea, B., Bayet, E., et al. 2005, *A&A*, 441, 961
- Lanz, L., Ogle, P. M., Alatalo, K., & Appleton, P. N. 2016, *ApJ*, 826, 29
- Lapham, R. C., Young, L. M., & Crocker, A. 2017, *ApJ*, 840, 51
- Leroy, A. K., Walter, F., Brinks, E., et al. 2008, *AJ*, 136, 2782
- Leroy, A. K., Walter, F., Sandstrom, K., et al. 2013, *AJ*, 146, 19
- Li, A., & Draine, B. T. 2001, *ApJ*, 554, 778
- Loubser, S. I., & Sánchez-Blázquez, P. 2011, *MNRAS*, 410, 2679
- Lu, N., Zhao, Y., Díaz-Santos, T., et al. 2017, *ApJS*, 230, 1
- Malhotra, S., Hollenbach, D., Helou, G., et al. 2000, *ApJ*, 543, 634
- Malhotra, S., Kaufman, M. J., Hollenbach, D., et al. 2001, *ApJ*, 561, 766
- Martig, M., Bournaud, F., Teyssier, R., & Dekel, A. 2009, *ApJ*, 707, 250
- McDermid, R. M., Alatalo, K., Blitz, L., et al. 2015, *MNRAS*, 448, 3484
- Moshir, M., et al. 1990, *IRAS Faint Source Catalogue*, version 2.0 (1990)
- Negishi, T., Onaka, T., Chan, K.-W., & Roellig, T. L. 2001, *A&A*, 375, 566
- Nesvadba, N. P. H., Boulanger, F., Salomé, P., et al. 2010, *A&A*, 521, A65
- Noll, S., Burgarella, D., Giovannoli, E., et al. 2009, *A&A*, 507, 1793
- Nyland, K., Young, L. M., Wrobel, J. M., et al. 2016, *MNRAS*, 458, 2221
- Oberst, T. E., Parshley, S. C., Stacey, G. J., et al. 2006, *ApJ*, 652, L125
- Oberst, T. E., Parshley, S. C., Nikola, T., et al. 2011, *ApJ*, 739, 100

- Ogle, P., Antonucci, R., Appleton, P. N., & Whysong, D. 2007, *ApJ*, 668, 699
- Onishi, K., Iguchi, S., Davis, T. A., et al. 2017, [arXiv:1703.05247](#)
- Osterbrock, D. E. 1989, *Astronomy*, 17, 102
- Ott, S. 2010, *Astronomical Data Analysis Software and Systems XIX*, 434, 139
- Parkin, T. J., Wilson, C. D., Schirm, M. R. P., et al. 2013, *ApJ*, 776, 65
- Parkin, T. J., Wilson, C. D., Schirm, M. R. P., et al. 2014, *ApJ*, 787, 16
- Peng, C. Y., Ho, L. C., Impey, C. D., & Rix, H.-W. 2002, *AJ*, 124, 266
- Peng, C. Y., Ho, L. C., Impey, C. D., & Rix, H.-W. 2010, *AJ*, 139, 2097
- Pilbratt, G.L., Riedinger, J. R., Passvogel, T. et al. 2010, *A&A*, 518, L1
- Poglitsch, A., Waelkens, C., Geis, N., et al. 2010, *A&A*, 518, L2
- Pound, M. W., & Wolfire, M. G. 2008, *Astronomical Data Analysis Software and Systems XVII*, 394, 654
- Roth, M. M., Kelz, A., Fechner, T., et al. 2005, *PASP*, 117, 620
- Sanders, D. B., & Mirabel, I. F. 1996, *ARA&A*, 34, 749
- Sargsyan, L., Samsonyan, A., Lebouteiller, V., et al. 2014, *ApJ*, 790, 15
- Savage, B. D., & Sembach, K. R. 1996, *ARA&A*, 34, 279
- Serra, P., Oosterloo, T., Morganti, R., et al. 2012, *MNRAS*, 422, 1835
- Shi, Y., Helou, G., Yan, L., et al. 2011, *ApJ*, 733, 87
- Shi, Y., Armus, L., Helou, G., et al. 2014, *Nature*, 514, 335
- Shi, Y., Yan, L., Armus, L., et al. 2018, [arXiv:1801.00888](#)
- Smethurst, R. J., Lintott, C. J., Simmons, B. D., et al. 2016, *MNRAS*, 463, 2986
- Smith, M. W. L., Gomez, H. L., Eales, S. A., et al. 2012, *ApJ*, 748, 123
- Stacey, G. J., Geis, N., Genzel, R., et al. 1991, *ApJ*, 373, 423
- Tacchella, S., Carollo, C. M., Renzini, A., et al. 2015, *Science*, 348, 314

- Temì, P., Brighenti, F., & Mathews, W. G. 2009, *ApJ*, 695, 1
- Temì, P., Brighenti, F., & Mathews, W. G. 2009, *ApJ*, 707, 890
- Temì, P., Brighenti, F., & Mathews, W. G. 2007a, *ApJ*, 660, 1215
- Temì, P., Brighenti, F., & Mathews, W. G. 2007b, *ApJ*, 666, 222
- Tielens, A. G. G. M., & Hollenbach, D. 1985, *ApJ*, 291, 722
- Toomre, A. 1964, *ApJ*, 139, 1217
- Tremonti, C. A., Heckman, T. M., Kauffmann, G., et al. 2004, *ApJ*, 613, 898
- Veilleux, S., & Osterbrock, D. E. 1987, *ApJS*, 63, 295
- Verheijen, M. A. W., Bershadý, M. A., Andersen, D. R., et al. 2004, *Astronomische Nachrichten*, 325, 151
- Wolfire, M. G., Tielens, A. G. G. M., & Hollenbach, D. 1990, *ApJ*, 358, 116
- Xiao, M.-Y., Gu, Q.-S., Chen, Y.-M., & Zhou, L. 2016, *ApJ*, 831, 63
- Young, L. M., Bureau, M., Davis, T. A., et al. 2011, *MNRAS*, 414, 940
- Young, L. M., Scott, N., Serra, P., et al. 2014, *MNRAS*, 444, 3408
- Zhao, Y., Lu, N., Xu, C. K., et al. 2013, *ApJ*, 765, L13
- Zhao, Y., Lu, N., Xu, C. K., et al. 2016a, *ApJ*, 819, 69
- Zhao, Y., Yan, L., & Tsai, C.-W. 2016b, *ApJ*, 824, 146
- Zubko, V., Dwek, E., & Arendt, R. G. 2004, *ApJS*, 152, 211

Table 1. A summary of the *Herschel* PACS and SPIRE Photometric Observations

Band (μm)	Beam FWHM Size (arcsec)	Pixel Size (arcsec)	Color Correction	Aperture Correction	Flux (Jy)
100	7.7	1.6	1.000	1.271	6.68 ± 0.34
160	12	3.2	1.004	1.271	7.27 ± 0.37
250	18.1	6	0.9121	1.256	2.84 ± 0.45
350	24.9	10	0.9161	1.256	1.09 ± 0.12
500	36.4	14	0.9005	1.256	0.35 ± 0.10

Table 2. Fine-structure Lines Observed with the PACS and SPIRE Spectrometer

Line	λ (μm)	ObsID	Obs Date	Spec. Resolution (km s $^{-1}$)	Angular Resolution (arcsec)	Flux (10^{-17} W m $^{-2}$)	FWHM (km s $^{-1}$)
[O I] 3P_1 – 3P_2	63.18	1342223367	2011 Jun 30	~ 86	~ 9.4	< 2.48	...
[N II] 3P_2 – 3P_1	121.90	1342234055	2011 Dec 11	~ 290	~ 10	14.09 ± 1.98	279, 221
[C II] $^2P_{3/2}$ – $^2P_{1/2}$	157.74	1342234055	2011 Dec 11	~ 238	~ 11.5	48.09 ± 0.84	248, 251
[N II] 3P_1 – 3P_0	205.18	1342247121	2012 Jun 18	~ 297	~ 17	7.24 ± 0.10	568
[C I] 3P_2 – 3P_1	370.42	1342247121	2012 Jun 18	~ 536	~ 36	0.40 ± 0.05	...

Note. — Column (1): atomic fine-structure line; columns (2): wavelength; columns (3): observation ID; column (4): observation date; column (5) and (6): spectral resolution and angular resolution from the PACS Observer’s Manual and SPIRE Handbook; column (7): measured fluxes of each atomic fine-structure line for NGC 3665; column (8): intrinsic line width.

Table 3. Photometry

Properties (1)	FUV (2)	NUV (3)	u (4)	g (5)	r (6)	i (7)	z (8)
Flux (mJy)	0.28 ± 0.02	1.07 ± 0.02	11.10 ± 0.03	58.50 ± 0.11	123.00 ± 0.23	187.00 ± 0.35	263.00 ± 0.48
J (9)	H (10)	K_s (11)	$I12_{\mu m}$ (12)	$I25_{\mu m}$ (13)	$I60_{\mu m}$ (14)	$I100_{\mu m}$ (15)	
567.00 ± 4.72	692.00 ± 7.04	564.00 ± 7.32	112.00 ± 20.10	162.00 ± 21.20	1920.00 ± 115.00	6340.00 ± 317.00	

Note. — Column (1): flux in unit of mJy; columns (2)-(3): flux of the *GALEX* far-UV (FUV) and near-UV (NUV) band, respectively; columns (4)-(8): flux of the SDSS u , g , r , i , and z band, respectively; columns (9)-(11): flux of the 2MASS J , H , and K_s band, respectively; columns (12)-(15): fluxes of the four *IRAS* bands.

Table 4. Derived properties from SED Fitting

$\log M_*$ (M_\odot)	$\log L_d$ (L_\odot)	$\log M_d$ (M_\odot)	T_W^{BC} (K)	T_C^{ISM} (K)	$\log M_{\text{gas}}$ (M_\odot)	M_{gas}/M_d	$\log L_{\text{TIR}}$ (L_\odot)
$10.79^{+0.07}_{-0.02}$	$9.90^{+0.01}_{-0.03}$	$6.85^{+0.04}_{-0.05}$	$55.81^{+3.65}_{-9.05}$	$22.86^{+0.50}_{-0.33}$	$9.11 \pm 0.01^{\text{a}}$	182	$9.88 \pm 0.02^{\text{b}}$

Note. — The column from left to right are: stellar mass, dust luminosity, dust mass, temperature of warm dust component in stellar birth clouds, temperature of cold dust component in diffuse ISM, total molecular gas mass, ratio of gas mass to dust mass, and total infrared luminosity. Uncertainties from MAGPHYS are the 16th-84th percentile range of the likelihood distribution from SED fitting.

^aThe total molecular gas mass is from the CARMA observations (Alatalo et al. 2013).

^bThe total infrared luminosity is integrated from SED best-fitting model between 8 and 1000 μm , with the error obtained from a Monte Carlo simulation.

Table 5. Results from the PDR model

Case	$\log n$ (cm^{-3})	$\log G_0$ ($1.6 \times 10^{-3} \text{ erg cm}^{-2} \text{ s}^{-1}$)
Uncorrected ^a	3.75	-0.25
Corrected ^b	4.00	-0.25

^aThe uncorrected values are derived from the best fit, including the observed [C II] only from the neutral gas region, all observed [O I]63 emission and F_{TIR} .

^bThe corrected values contain the [C II] divided by a factor of 1.4 in the neutral gas region and the F_{TIR} reduced by 2.0.

Table 6. Results from the r -band bulge-disk decomposition

Component	m_r (mag)	R_e (arcsec)	Sérsic index	b/a	PA (deg)	χ^2/nu
one Sérsic	11.18	50.15	3.81	0.78	28.12	0.95

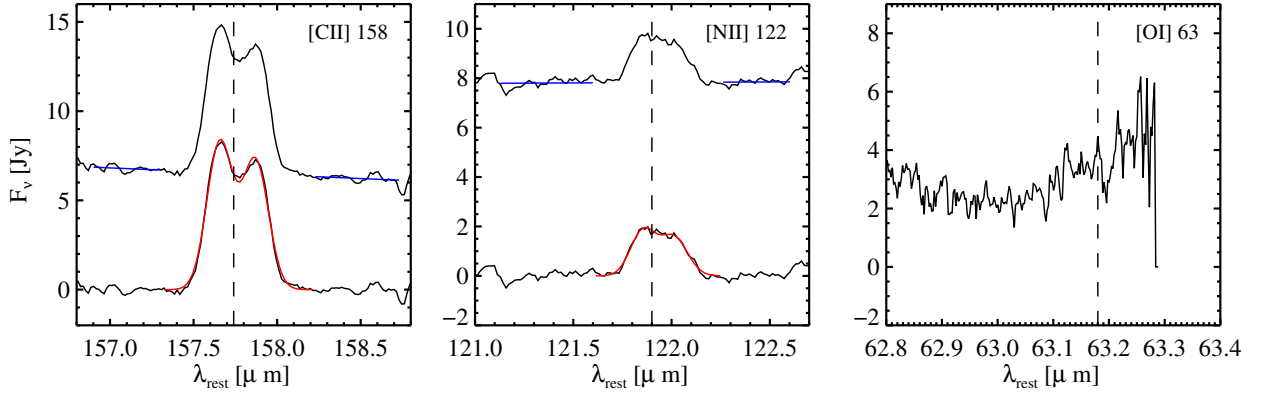


Fig. 1.— The [C II] 158 μm , [N II] 122 μm , and [O I] 63 μm spectra combined within central 3×3 spaxels. In the left two panels, the top and bottom black lines show observed spectra and emission lines with two Gaussian components fitted in red, respectively. The continuum emission was fitted by first-order polynomial in blue. The right panel shows observed spectra of [O I] 63 μm .

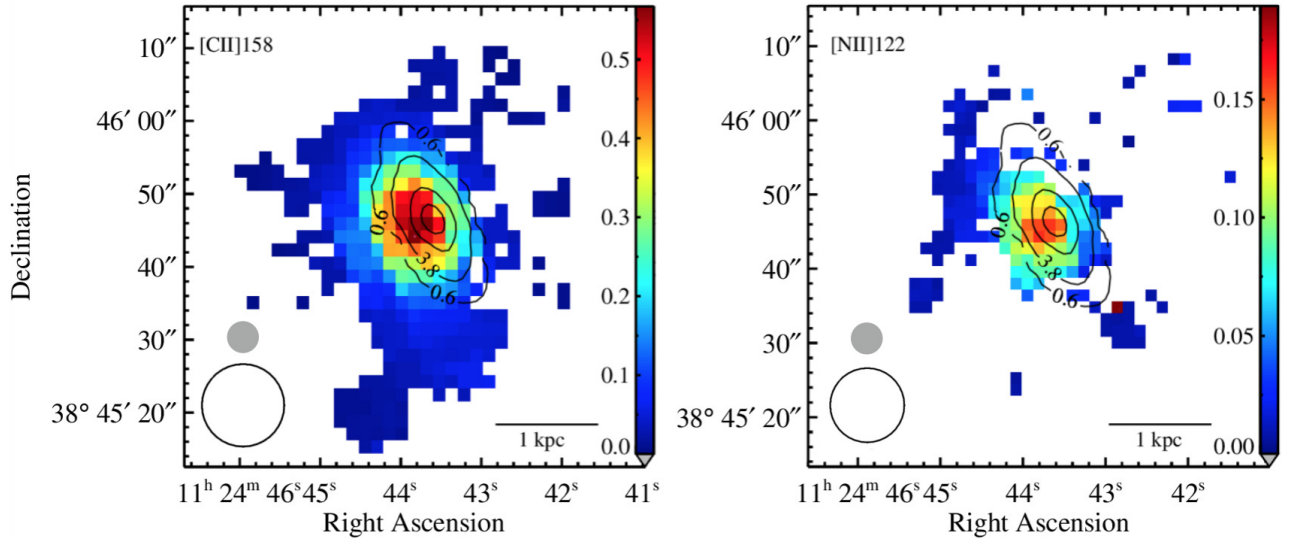


Fig. 2.— The $[\text{C II}] 158 \mu\text{m}$ and $[\text{N II}] 122 \mu\text{m}$ integrated intensity maps (color scale), overlaid with contours of $\text{CO}(1-0)$ integrated intensity (moment0) from CARMA. We have used the 3σ cut to highlight the robust detections. Contour levels are 2.5, 16, 50, 84 per cent of the peak, while the peak flux is $24.04 \text{ Jy beam}^{-1} \text{ km s}^{-1}$. The color table on the right of each panel provides the integrated flux scale of $[\text{C II}] 158 \mu\text{m}$ and $[\text{N II}] 122 \mu\text{m}$, respectively, with the unit in $10^{-17} \text{ W m}^{-2}$. The synthesized beam of *Herschel* and CARMA are shown in the bottom-left corner, with black open circle and grey filled circle, respectively. North is up, and east is to the left.

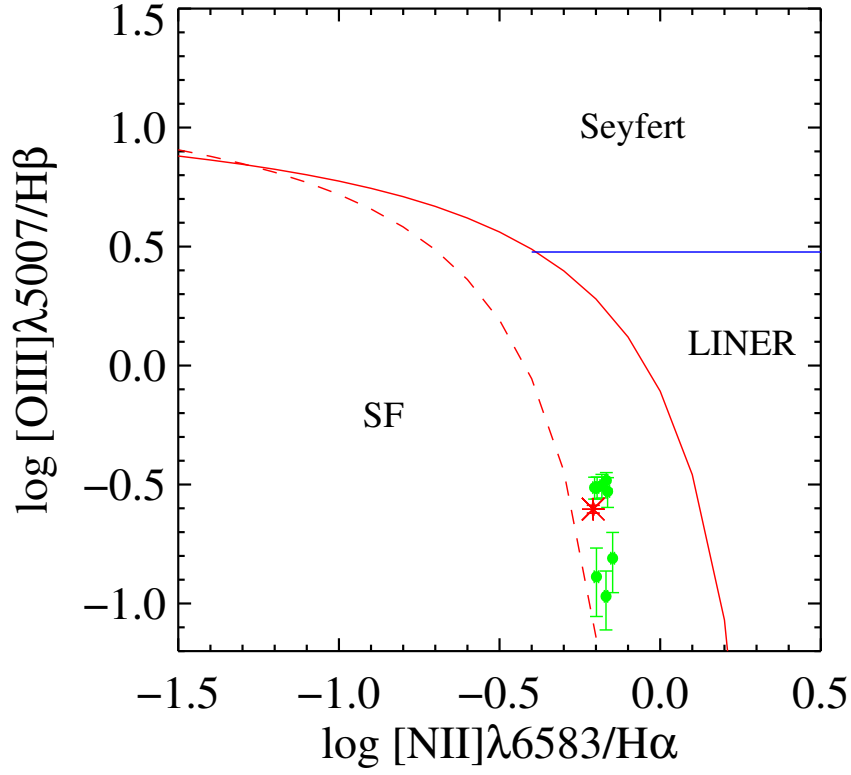


Fig. 3.— The BPT diagram in the central $3'' \times 3''$ spaxels. Green points are each individual spaxel, which lie between the red solid line (Kewley et al. 2001) and the red dash line and blue line (Kauffmann et al. 2003). Red star shows 9 spaxels as a whole. Both the green points and red star, with the uncertainties, lie in the composite region in this diagnostic diagram.

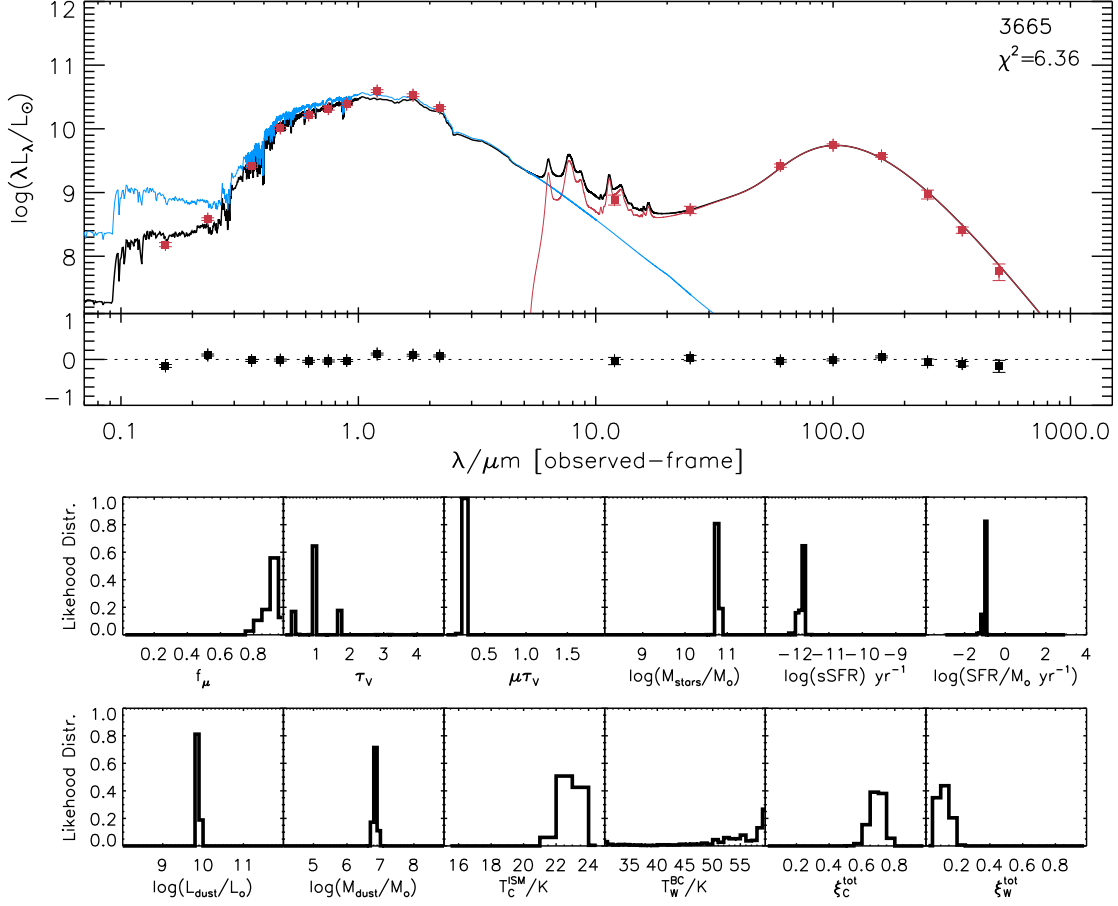


Fig. 4.— Best MAGPHYS model fits (black line) to the observed SED (red points) of the NGC 3665. The data are composed of two *GALEX*, five SDSS, three 2MASS, three *IRAS*, two PACS, and three SPIRE bands. In the top panel, the blue line represents the unattenuated stellar population spectrum, and the red line represents the dust emission. For each observational point, the red error bar indicates the measurement error, which also shown with the residuals $(L_{\text{obs}} - L_{\text{mod}})/L_{\text{obs}}$ in black. The bottom twelve minor panels show the likelihood of physical parameters derived from fits to the observed spectral energy distribution, including the fraction of the total dust luminosity accounted by dust in the diffuse ISM (f_{μ}), the total V -band optical depth of the dust (τ_V), the V -band optical depth of the dust in the diffuse ISM ($\mu\tau_V$), stellar mass, specific star formation rate, star formation rate, total stellar luminosity absorbed by dust, the equilibrium temperature of cold dust in the diffuse ISM (T_C^{ISM}), the equilibrium temperature of warm dust in the stellar birth clouds (T_W^{BC}), the fractional contribution by cold dust to the total dust luminosity (ξ_C^{tot}), and the fractional contribution by warm dust to the total dust luminosity (ξ_W^{tot}).

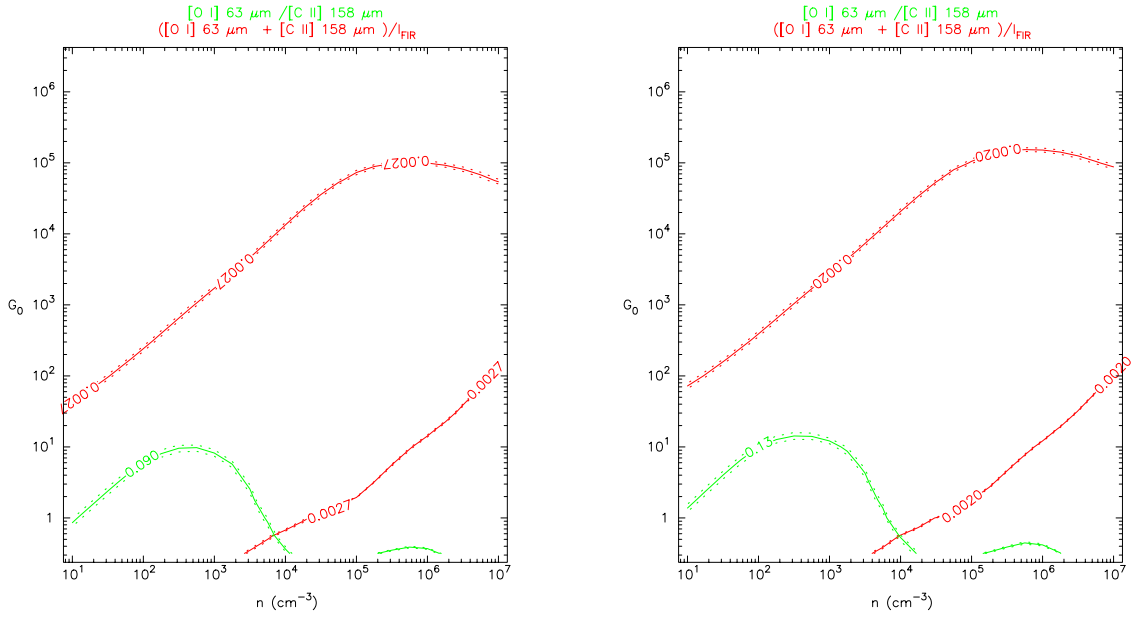


Fig. 5.— The line ratio curves created from on-line PDRT, as a function of the hydrogen nucleus density, n , and the strength of FUV radiation field, G_0 . Solid lines represent computed ratios, and the dashed lines represent error bar. The intersections of two ratio curves indicate the best-fit quantities. The left/right panels are corresponding to the uncorrected/corrected results, respectively, in Table 5.

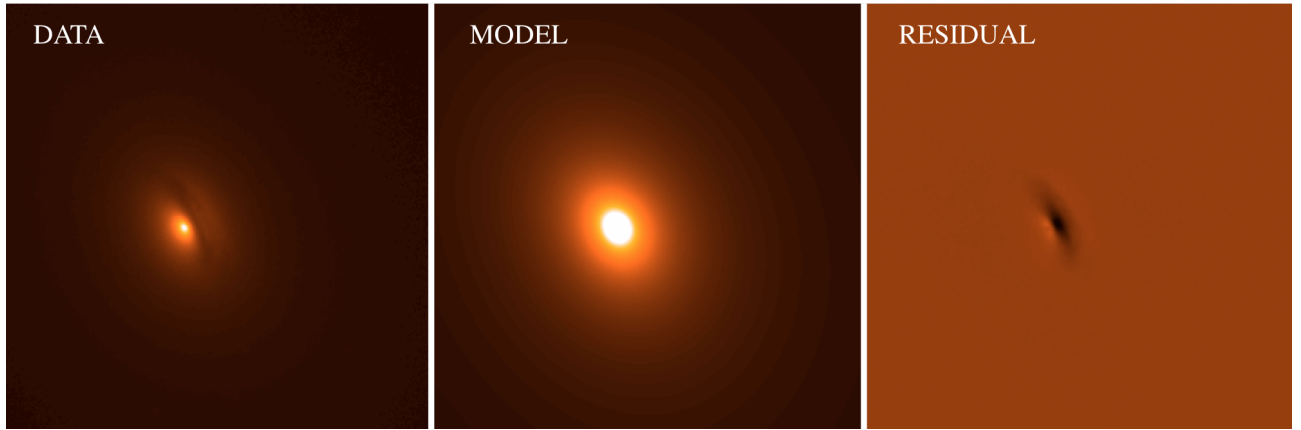


Fig. 6.— The 2D bulge-disk decomposition of NGC 3665 with GALFIT. Panels from left to right are r-band observed image, model image, and model-subtracted residual image. The black region in residual image shows a dust structure near the galaxy center, which has been masked out before the fitting.